

ORIGINAL ARTICLE

Biaxial stress controlled three-dimensional helical cracks

Li Wang^{1,4,5}, Xiang-Ying Ji^{2,5}, Nü Wang³, Jing Wu³, Hua Dong^{1,4}, Jiexing Du³, Yong Zhao³, Xi-Qiao Feng² and Lei Jiang^{1,3}

Cracks are Janus-faced, which cause material failure on one hand and serve as a powerful approach for material processing on the other. To predict cracks and control them in a desired manner, foundational fracture mechanisms are continuously being pursued, based on simplified modes of planar cracks. In reality, cracks usually occur in a three-dimensional (3D) irregular manner. Prediction of 3D fractures is of particular significance for understanding the fundamental fracture mechanisms. However, controlling cracks in typical 3D modes is rare. Here we report that controllable 3D helical cracks on heterogeneous spindle knots are induced by biaxial thermal stresses. The thermal expansion mismatch between the tough core and brittle shell during the heating process generates biaxial stresses in the axial and circumferential directions. Surface cleavage and interface delamination driven by the release rate of elastic strain energy are harmonized due to the unique spindle geometry and cooperate to produce a 3D helical crack. This finding is helpful for understanding complex cracking mechanisms and provides a promising prospect for controlling or eliminating 3D cracks.

NPG Asia Materials (2012) 4, e14; doi:10.1038/am.2012.26; published online 20 April 2012

Keywords: biaxial stress; crack; helical

INTRODUCTION

Cracks are often regarded as an undesirable phenomenon, because they may induce material failure, breakdown of devices and collapse of buildings. For prediction and prophylaxis of fracture, foundational fracture mechanisms are established by analyzing simple planar cracks. Various methods from continuous^{1,2} to atomistic mechanics^{3,4} have been developed to investigate the failure of materials spanning a wide range of temporal and spatial scales.^{5–7} A crack is initiated when the stresses exceed the material strength and will tend to propagate along whichever path allows the most energy to be released. According to the type of applied stress, cracks are typically classified into three different modes: opening, sliding and tearing; each propagates straight through a homogenous material. If cracks are under mixed-mode loading,⁸ such as tensile and shear stresses, they often propagate in a curved or kinked manner.^{9–12} Under certain conditions, the kinking paths may continue regularly to form various crack patterns.^{13,14} For example, two-dimensional spiral or sinusoidal cracks can arise in the dried crusts of aqueous suspensions¹⁵ or in glass slides under gradient temperature fields.^{16,17} In contrast with

two-dimensional planar cracks, three-dimensional (3D) cracks are more universal and controlling. Cracks in normal 3D modes are of significance not only in theoretical studies, but also for practical applications. In engineering, there have been many efforts devoted to obtaining cracks in an orderly fashion. Until now, experimental and theoretical investigations for controlling cracks in normal 3D modes have been rare. Here, controllable 3D helical cracks on heterogeneous spindle knots (the knots with spindle shape) induced with biaxial thermal stresses are reported, which are of great significance for fracture mechanisms and material fracture techniques.

MATERIALS AND METHODS

A 3D helical crack on a heterogeneous spindle knot is fabricated as follows. First, a thin layer of a titania/polymer sol was dip-coated onto a columnar glass microfiber with a uniform smooth surface (Supplementary Figure S1, Supplementary Information). Intact heterogeneous spindle knots^{18,19} are created using a simple dip-coating procedure, which takes advantage of the Raleigh instability²⁰ of the liquid layer. The dried droplets form a series of periodic core-shell spindle knots. When the dried spindle knots are calcined,

¹Beijing National Laboratory for Molecular Sciences (BNLMS), Key Laboratory of Organic Solids, Institute of Chemistry, Chinese Academy of Sciences, Beijing, China; ²AML, Department of Engineering Mechanics, Tsinghua University, Beijing, China; ³Key Laboratory of Bio-Inspired Smart Interfacial Science and Technology of Ministry of Education, School of Chemistry and Environment, Beihang University, Beijing, China and ⁴Graduate University of the Chinese Academy of Sciences, Beijing, China

⁵These authors contributed equally to this work.

Correspondence: Professor Y. Zhao, Key Laboratory of Bio-Inspired Smart Interfacial Science and Technology of Ministry of Education, School of Chemistry and Environment, Beihang University, Beijing 100191, China.

E-mail: zhaoyong@iccas.ac.cn

or Professor X-Q. Feng, AML, Department of Engineering Mechanics, Tsinghua University, Beijing 100084, China

E-mail: fengxq@tsinghua.edu.cn

Received 3 February 2012; revised 26 February 2012; accepted 27 February 2012

a 3D helical crack forms on each knot as a consequence of thermal biaxial stresses. A detailed preparation process, is as follows:

- (1) Preparation of sol-gel: Pluronic P123 (1 g) was dissolved in 10 g of an ethanol and 1-butanol solution (1:1 by weight). Subsequently, 0.018 mol precursor (for details, see the Supplementary Information) and 2.4 g HCl/acetic acid of solution were added under vigorous stirring for 30 min and aged for 24 h.
- (2) Formation of helical crack: A glass microfiber was ultrasonically cleaned for 5 min in purified water, acetone and then ethanol. After drying, the microfiber was immersed in the sol-gel solution with a dip-coater (WPTL5-0.01, Shenyang Kejing Instrument Corporation, Shenyang, China) at a velocity of 20 mm min^{-1} , held for 1 min, and then horizontally drawn out at a velocity of 40 mm min^{-1} . A thin metal-oxide sol film formed on the fiber; the liquid film spontaneously broke up into a series of tiny barrel solution droplets within several seconds. After these droplets dried, the periodic spindle knots formed on the microfiber. The spindle-knotted samples were aged in a high humidity chamber (RH > 60%) at 20°C for 24 h. Finally, the dried knots were calcined with a heating rate of $0.5^\circ\text{C min}^{-1}$ from ambient temperature up to 500°C , and held for 4 h to remove any organic compounds.
- (3) Optical microscopy characterization of helical cracks: The sample was placed on a clean slide glass ($25.4 \times 76.2 \times 1.2 \text{ mm}$) and was observed using transmitted light on an Olympus microscopy system Model BX51 (Olympus, Tokyo, Japan).

Scanning electron microscopy characterization of helical cracks: Scanning electron microscopy images were collected with an accelerating voltage of 3 kV (JAPAN Electron OPTICS LABORATORY Ltd., Tokyo, Japan, SEM 6700). The helical angle distributions of the cracks were determined using image analysis techniques.

Micro X-ray computer tomography (Micro-XCT) of helical cracks: Specimens were first sealed with a liquid epoxy to prevent damage. After pouring in the liquid epoxy, the samples were placed under vacuum for 1 h to remove air bubbles and then cured at 80°C for 24 h. The solidified specimens were frozen in liquid nitrogen and cut into columns (3 mm in length with a diameter of 1.5 mm). The whole operation was aided by a

BX51 microscope. The microscale morphology of the helix was observed using a 3D MicroXCT-200 (Xradia Inc., Concord, MA, USA) at $40\times$ magnification. Computed tomography facilitated the 3D viewing of the object. Transmission X-ray imaging of the specimen was performed using X-rays at 90 kV and 8 W.

- (4) Theoretical analysis: Numerical simulations of the stress distributions in the specimens were calculated using the finite element method.

RESULTS AND DISCUSSION

Figure 1 shows the morphologies of spindle knots before and after calcination. The dip-coated core-shell spindle knots have intact smooth surfaces before calcination (Figure 1a). After calcination, screw-shaped cracks appeared on the spindle knots (Figure 1b). Detailed morphologies of a typical helical crack (Figures 1c–e) show that the crack spacing is relatively uniform along the entire fracture orbit. The crack penetrates the entire shell thickness, whereas the inner fiber remains intact (Figure 1c). Magnified images (Figures 1d and e) reveal that the cleavage surface is smooth, indicating a brittle fracture governed by linear elastic fracture mechanics.²¹ It is evident that the interface between the shell and the fiber core has entirely delaminated after cracking (Figure 1e). These results imply that helical crack propagation, involving both surface cracking and interface delamination, should be motivated by a single steady mechanism.

It is well known that heat treatments will result in thermal stresses in a material^{16,17} and that cracks can arise when the stress intensity exceeds the strength of the material. Such cracks usually propagate along various unpredictable random patterns, such as the notorious cracked glazes on pottery; this is also the case for a glass/titania core-shell fiber with uniform shell thickness that undergoes a heating process (Supplementary Figure S2, Supplementary Information). On the spindle core-shell specimen (Figure 1c), however, highly regular 3D helical cracks emerged after calcination. We therefore assume that the special spindle morphology⁴ and heterogeneous interface^{12,22,23} have important roles in shaping the unique helical crack.

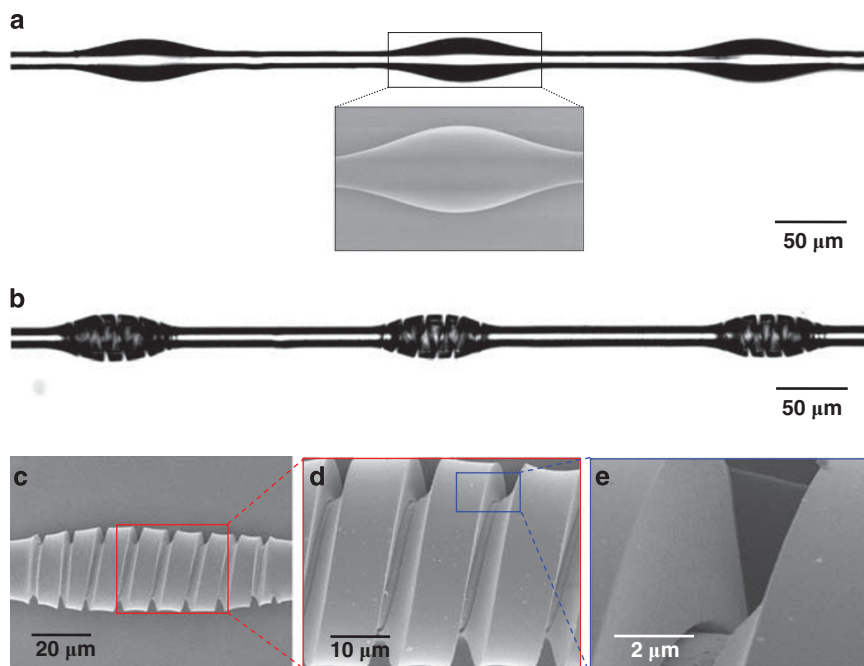


Figure 1 Intact and helically cracked spindle knots before and after calcination. (a) Optical image of periodic spindle knots wrapped around a uniform smooth glass microfiber. Inset of scanning electron microscopy image of a spindle knot showing the intact smooth surface. (b) Screwed microcracks formed on the spindle knots after calcination. (c) A typical helically cracked spindle knot with seven coils. (d, e) Magnified views of the helical crack showing the brittle fracture and completely interfacial delamination between the core and shell.

To reveal the underlying fracture mechanism, the von Mises equivalent stress distribution in the specimen was calculated.²⁴ Figure 2a presents the obtained stress distribution state, which shows that the stresses are more concentrated at the two spindle ends than in the middle due to the shell thickness gradient of the spindle knot.

According to the Griffith fracture criterion, the driving force for crack propagation is the release rate of the elastic strain energy per unit crack advancement G . Only when G is high enough to meet the fracture resistance G_c of the material can the crack propagate in brittle materials.²⁵ It is apparent that a helical tunneling crack can continuously carve a curved surface into a core-shell structure. At the same time, the single-sided interface delamination between the created helix and the shell is facilitated by the helical tunneling crack. The interface delamination extends the entire helix pitch and advances simultaneously with the surface crack propagation, resulting in a steady channel cracking delamination failure mode. According to these indications, a simulated scenario of how the crack propagates is hereby proposed. For a heterogeneous system with a brittle shell and a tough core, fracture would start at the free surface of the shell and then tunnel through the specimen. The crack should initiate randomly at either of the two ends (Figure 2b). When the crack reaches the interface,^{22,26} delamination occurs between the outer shell and the inner fiber (Figure 1e), and complete detachment appears after the crack tip has advanced (Figure 2c). In this model, we use a cylinder with radius R with the shell and interface under uniform biaxial stresses, with the two principal stresses, σ_1 and σ_2 , along the axial and circumferential directions, respectively (Figure 2d). The assumed 3D crack in our model has been verified using Micro-XCT, as shown in Figure 3. The section image in the axial direction (Figure 3b) shows the planar spiral notch of a crack (also see Supplementary Movie S1 and Supplementary Figure S3, Supplementary Information), which is in good agreement with our simulations (Figure 2c). Because of the X-ray contrast between the heterogeneous core and shell, the cracked spindle knot can be viewed as a spring by technically fading the glass core in the Micro-XCT (Figure 3c and Supplementary Movie S2 in the Supplementary Information).

Considering the unique shape of the helical crack, the total energy release rate during this process includes the contributions of the coupling channel cracking and interface delamination. If there was no interface delamination, the surface crack would be a typical opening mode crack and grow along the direction perpendicular to the principal stress, rather than along the observed helical orbit. The interface delamination is therefore critical to the formation of the helical crack. Because of the spindle configuration (Figure 1a), the axial normal stress is slightly larger than that in the circumferential direction. Under such a stress state, a circumferential or axial crack having an inclination angle of 0° or 90° will be governed by one of the two mechanisms for maximum energy release rate, with the other having a supporting role. As a result, the crack will compromise into an optimal helix shape that maximizes the strain energy release rate under a specific biaxial stress state, as observed in our experiments.

We assume that a circumferential crack with length $2c$ initiates at one end of the glass fiber. The biaxial stress kinks the crack along an inclination angle θ (Figure 2b) with respect to the circumferential direction, whereas the interface is simultaneously delaminated. Let G_1 and G_2 denote the two contributions of the energy release rate induced by surface cleavage and interface delamination, respectively, which will be calculated separately. As previously mentioned, G_1 will be maximized if the surface crack propagates along a circumferential direction or, in other words, in a pure opening mode. For this case, the specimen will be fragmented into an array of doughnut shapes without interface delamination. When interface delamination is considered, however, the real fracture process becomes the releasing of not only the elastic strain energy corresponding to the axial stress σ_1 , but also the release of strain energy from σ_2 . An increasing value of θ results in a higher energy release rate G_2 despite the relative decrease of G_1 .

The energy release rate of the surface crack G_1 is calculated as follows. When the first principal stress is along the axial direction, for a pre-existing circumferential crack of length $2c$, the stress intensity factor (SIF) for opening mode loading K_I is proportional to σ_1 and the square root of the half crack length \sqrt{c} . The coefficient is related to the cylinder radius R .²⁷ An approximate description of K_I as

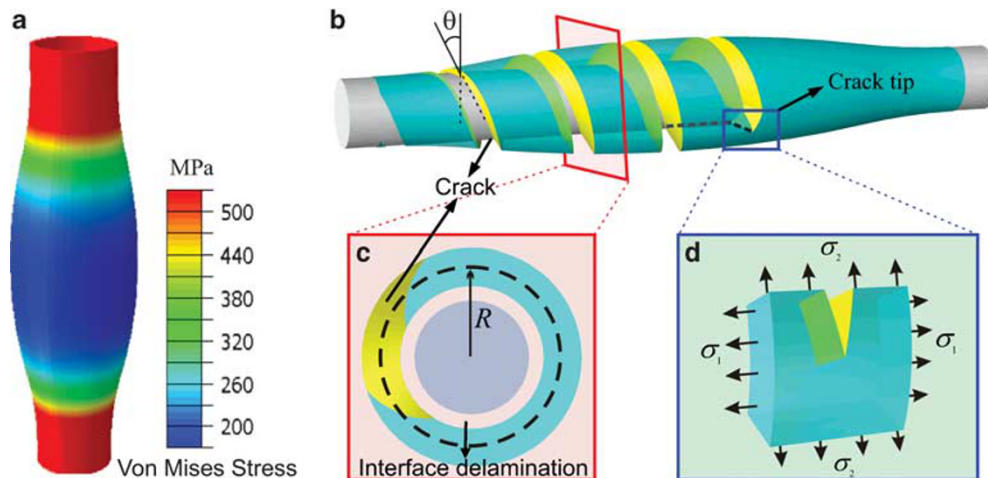


Figure 2 (a) Von Mises stress distribution in the outer spindle shell (MPa). (b–d) Scheme of the cracking model. (b) The helical cracking orbit and the forming helical angle θ with the circumference plane. As the crack tip advances, the interface delaminates at an almost identical speed. Interface delamination is continuous and synchronous with surface crack propagation. (c) Imaginary cross-section of the cracked sample with a surface crack and interface delamination. After cracking, the outer shell detaches from the inner fiber. (d) The biaxial stresses in axial and circumferential directions around the cracking tip are mainly caused by thermal expansion mismatch.

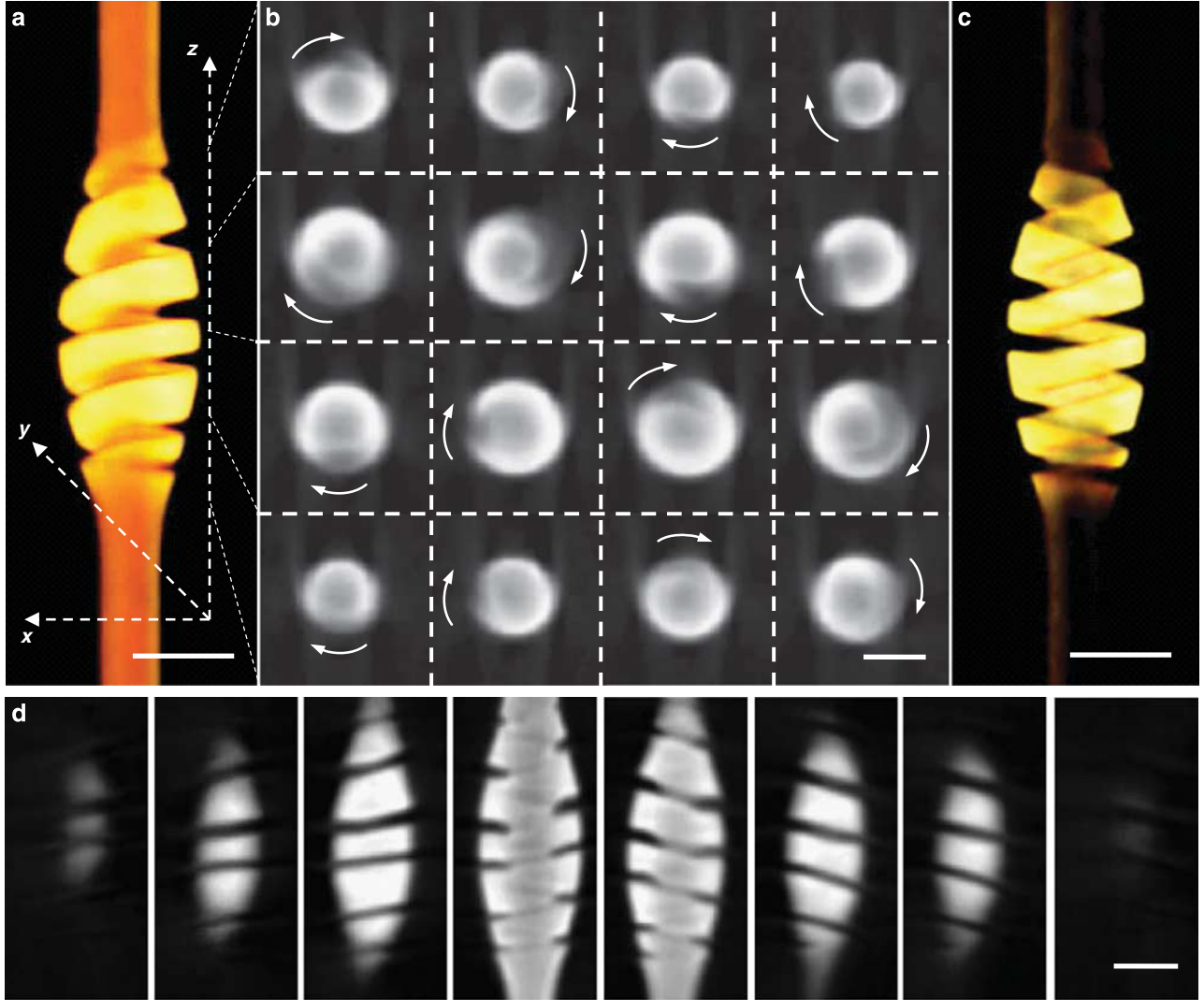


Figure 3 Detailed 2D and 3D images of a helical crack from different perspectives by Micro-XCT. **(a)** A 3D perspective image of a helically cracked spindle knot on a glass microfiber. The x - y plane is perpendicular to the fiber axis, whereas the z axis is parallel to the fiber axis. **(b)** 2D sectional images in the x - y plane along the z axis from one end of the fiber to the other. The arrows indicate the coiling directions of the crack. **(c)** A 3D perspective image of a helically cracked spindle knot resembling a spring after the glass microfiber is faded when using X-ray imaging contrast between the core and shell materials. **(d)** 2D sectional images in the x - z plane along the y axis. Scale bars = 20 μm .

$K_I = \sigma_1 \sqrt{\pi c} [1 + \Psi(c/R)]$ is taken to let the factor reduce safely to the planar condition with infinite R , where $\Psi(c/R)$ is a dimensionless function of c/R , which passes through the origin. Upon viewing an existing SIF solution for a crack in a thin wall of a cylindrical shell,^{28,29} we write $\Psi(c/R)$ as $m(c/R)^2$, where m reflects the influences of the shell thickness and the existence of the inner fiber. The SIF for sliding mode loading K_{II} is zero. For a kinking tip with an angle θ from the original route, the SIFs can be calculated as:

$$K_I(\theta) = K_I \cos^3 \frac{\theta}{2} - 3K_{II} \sin \frac{\theta}{2} \cos^2 \frac{\theta}{2},$$

$$K_{II}(\theta) = K_I \sin \frac{\theta}{2} \cos^2 \frac{\theta}{2} + K_{II} \cos \frac{\theta}{2} \left(1 - 3 \sin^2 \frac{\theta}{2}\right).$$

and the energy release rate by the surface crack becomes:

$$G_1 = \frac{K_I(\theta)^2 + K_{II}(\theta)^2}{\bar{E}} = \frac{K_I^2}{\bar{E}} \cos^4 \frac{\theta}{2} = \frac{\sigma_1^2}{\bar{E}} \pi c [1 + m(c/R)^2]^2 \cos^4 \frac{\theta}{2},$$

where \bar{E} is the effective elastic modulus.

The energy release rate of the interface delamination G_2 is calculated as follows. Assuming that as the crack tip advances, the zone between the current and previous coil debonds promptly. The larger the helix angle, the larger the delamination area. The energy released is that of the normal stress along the propagation direction of delamination, and namely, the cracking direction. The normal stress σ_n is computed as:

$$\sigma_n = [\sin \theta \quad \cos \theta] \begin{bmatrix} \sigma_1 & 0 \\ 0 & \sigma_2 \end{bmatrix} \begin{bmatrix} \sin \theta \\ \cos \theta \end{bmatrix} = \sigma_1 \sin^2 \theta + \sigma_2 \cos^2 \theta.$$

Thus, G_2 is derived as:

$$G_2 = \frac{1}{E} (\sigma_1 \sin^2 \theta + \sigma_2 \cos^2 \theta)^2 2\pi R \sin \theta.$$

The total energy release rate G is the summation of G_1 and G_2 . G is written in the following form:

$$G = 2\pi R \frac{\sigma_1^2}{E} \left[(\sin^2 \theta + t \cos^2 \theta)^2 \sin \theta + 2\eta \cos^4 \frac{\theta}{2} \right],$$

where $\eta = (c/R)[1 + m(c/R)^2]^{1/2}/4$ and $t = \sigma_2/\sigma_1$ are both dimensionless. The value η purely takes into account geometry and t takes the ratio of the two principal stresses, which represent the stress state. Clearly, for determined R and σ_1 , the optimal helix angle θ_0 that maximizes G , in which the angle of fracture follows, is determined jointly with η and t .

The most favorable helix angle for the crack propagation, denoted as θ^* , is determined by maximizing G , that is, $G(\theta^*) = \max(G(\theta))$. The variation tendency of the helix angle with respect to the stress ratio t bifurcates as η changes (Figures 4a and b). For η smaller than approximately 0.7, a large helix angle θ^* is favored when axial stress is dominant; the angle diminishes as σ_2 approaches σ_1 . Conversely, for a larger value of η , when the stress ratio σ_2/σ_1 rises from 0 to 1, a circumferential crack will form first, and the crack angle will gradually increase. These two contrary trends reflect the competition between the two coupled energy release mechanisms of channel cracking and interface delamination. When the geometric and stress state parameters are in the upper region of Figure 4c, one has $G_1 > G_2$, indicating that surface cleavage overwhelms interface delamination, whereas in the lower region, interface delamination dominates the cracking process. Comparing Figure 4c with the helix angle contour in Figure 4d, it can be concluded that the changing trend of the helix angle mainly depends on the predominant energy-releasing mechanism. When surface cleavage prevails, the energy of σ_1 is more likely to be released by a circumferential opening-mode crack. In contrast, if delamination predominates, the elastic energy will be mainly released by interface failure. The dominating regions of the two competing mechanisms are divided by a nearly constant value of η . Therefore, it is η , a function of c/R , that regulates the dominating fracture mechanism. Specifically, the structural and geometric characters determine the value of η and, in turn, the dominating mechanism. In contrast, the difference between the thermal expansion coefficients of the inner fiber and the outer shell dictates the intensity of the stress field at the crack tip and therefore represent the critical condition for

whether helical cracking occurs. Under different values of η , the helix angle determined by the two different mechanisms tend to converge as σ_2 approaches σ_1 , demonstrating the governing role of the biaxial stress state in the formation of the helical spring. When the two stresses approach one another, the helix angle will reach a value of approximately 20° to 30° , which is in accordance with the experiments in Supplementary Figure S4, Supplementary Information.

It is now clear that the helical crack arises from the biaxial stress and is motivated by the cooperation of surface cleavage and interface delamination. The special spindle shape of the core-shell knot facilitates the even release of the biaxial stresses, resulting in a 3D helical crack. By changing the shape of the spindle knots, and thus, the biaxial stresses, the number of helical coils can be easily regulated. According to the Raleigh instability of the polymer solution on a fiber, the shapes of the spindle knots are influenced by a number of parameters; for example, the viscosity of the coating solutions, the wettability of the core fiber and solution, and the pulling rate during the dip-coating process. Figures 5a–d shows helical cracks with 1, 4, 9 and 14 coils, respectively, demonstrating the high reliability and controllability of the biaxial stress fracture technique. The statistical results show that the number of helical coils increases in direct proportion to the length–diameter ratio of the spindle knots (Figure 5e). Thus, one can easily tune the number of coils by adjusting parameters, such as viscosity of the coating solution and the wettability of the core fiber.¹⁹ If a soft or elastic fiber is used as the core, no helical cracks will arise (Supplementary Figure S5, Supplementary Information). For this case, the thermal stresses are not sufficient to induce cracking. This further indicates that the helical crack mode should be governed by the biaxial stress state, under which a synergy of surface cracking and interface delamination drives the helical crack propagation. By removing the core fiber, micro-sized springs with different types of coils can be obtained (Figure 5f). These results suggest prospects for controlling the cracking mode during materials processing.³⁰

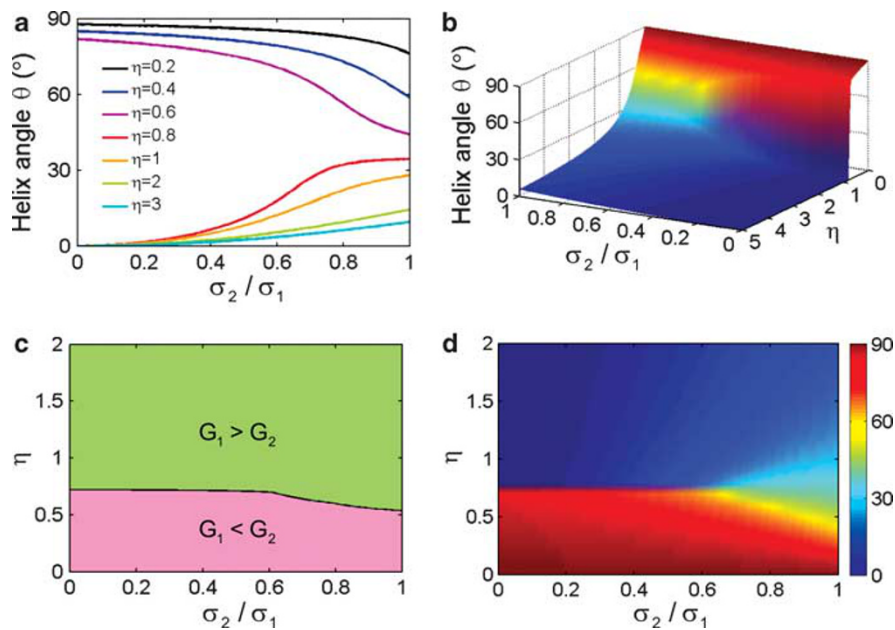


Figure 4 Variation of the helix angle θ with the dimensionless parameters $t = \sigma_2/\sigma_1$ and $\eta = \eta(c/R)$. (a) Variation of θ with σ_2/σ_1 with different values of η . (b) 3D map of θ as a function of σ_2/σ_1 and η . (c) Parameter regions of σ_2/σ_1 and η that dominate the two different cracking mechanisms. In the upper region (green), the energy released by surface cracking overwhelms that of interface delamination, whereas in the lower region (pink), interface delamination is dominant. (d) Contour map of θ with σ_2/σ_1 and η , showing the regions where the two cracking mechanisms prevail.

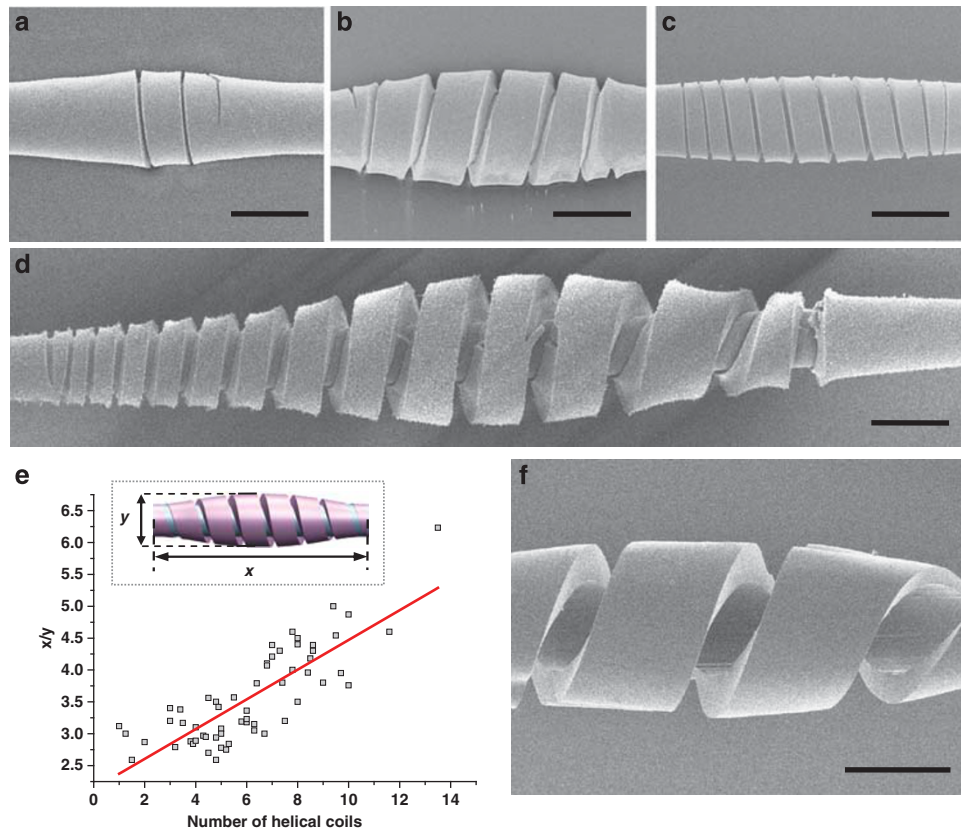


Figure 5 Helical cracks with controllable numbers of coils and the manufacturing of a microspring. (a–d) Helical cracks with 1, 4, 9 and 14 coils, respectively, demonstrating the high reliability and controllability of the biaxial stress fracture technique. (e) Direct proportion relationship between the length–diameter ratio of the spindle knot (x/y) and the number of helical coils. (f) Creation of a microspring through the removal of the core material. Scale bars = 20 μm .

As discussed above, the proposed crack mode should not be limited to certain specific kinds of fiber materials, but is applicable to many different materials systems if there is a thermal expansion coefficient difference between two heterogeneous materials. As expected, diverse helices of ceramics,³¹ including SiO_2 , Al_2O_3 , Fe_2O_3 and even mixed oxides, such as FeBiO_3 , have been successfully created (Supplementary Figure S6, Supplementary Information). Therefore, such a mechanism is prevalent for heterogeneous core-shell specimens with a brittle shell and a weak interface. This study not only widens our understanding of cracking phenomena, but also sheds light on the control and design of regular cracks with arbitrary dimensions.³² This cracking mode holds promise for applications in eliminating or controlling cracks during manufacturing processes.

CONFLICT OF INTEREST

The authors declare no conflict of interest.

ACKNOWLEDGEMENTS

We acknowledge the National Natural Science Foundation of China (21134003, 10732050, 21004002 and 21071148) and the State Basic Research Program of China (2012CB933200, 2010CB934700, 2010CB631005 and 2009CB930404) for continuing financial support.

- Cox, B.N., Gao, H., Gross, D. & Rittel, D. Modern topics and challenges in dynamic fracture. *J. Mech. Phys. Solids* **53**, 565–596 (2005).
- Hutchinson, J.W. & Suo, Z. Mixed mode cracking in layered materials. *Adv. Appl. Mech.* **29**, 63–191 (1992).

- Abraham, F.F., Walkup, R., Gao, H., Duchaineau, M., De La Rubia, T. D. & Seager, M. Simulating materials failure by using up to one billion atoms and the world's fastest computer: Brittle fracture. *Proc. Natl Acad. Sci. USA* **99**, 5777–5782 (2002).
- Gross, D., Muller, R., Muller, M., Xu, B. X. & Albe, K. On the origin of inhomogeneous stress and strain distributions in single-crystalline metallic nanoparticles. *Int. J. Mater. Res.* **102**, 743–747 (2011).
- Freund, L. B. *Dynamic Fracture Mechanics* 55–103 (Cambridge University Press, New York, 1990).
- Livne, A., Bouchbinder, E., Svetlizky, I. & Fineberg, J. The near-tip fields of fast cracks. *Science* **327**, 1359–1363 (2010).
- Bazant, Z. P., Le, J. L. & Bazant, M. Z. Scaling of strength and lifetime probability distributions of quasibrittle structures based on atomistic fracture mechanics. *Proc. Natl Acad. Sci. USA* **106**, 11484–11489 (2009).
- Pons, A. J. & Karma, A. Helical crack-front instability in mixed-mode fracture. *Nature* **464**, 85–89 (2010).
- Cotterell, B. & Rice, J. R. Slightly curved or kinked cracks. *Int. J. Fract.* **16**, 155–169 (1980).
- Gol'dstein, R. V. & Salganik, R. L. Brittle fracture of solids with arbitrary cracks. *Int. J. Fract.* **10**, 507–523 (1974).
- Adda-Bedia, M., Arias, R., Ben Amar, M. & Lund, F. Generalized Griffith criterion for dynamic fracture and the stability of crack motion at high velocities. *Phys. Rev. E* **60**, 2366–2376 (1999).
- Katzav, E., Adda-Bedia, M. & Derrida, B. Fracture surfaces of heterogeneous materials: A 2D solvable model. *Europhys. Lett.* **78**, 46006 (2007).
- Morel, S., Schmittbuhl, J., Bouchaud, E. & Valentin, G. Scaling of crack surfaces and implications for fracture mechanics. *Phys. Rev. Lett.* **85**, 1678–1681 (2000).
- Ponson, L., Bonamy, D. & Bouchaud, E. Two-dimensional scaling properties of experimental fracture surfaces. *Phys. Rev. Lett.* **96**, 035506 (2006).
- Cohen, Y., Mathiesen, J. & Procaccia, I. Drying patterns: sensitivity to residual stresses. *Phys. Rev. Lett.* **79**, 046109 (2009).
- Menouillard, T. & Belytschko, T. Analysis and computations of oscillating crack propagation in a heated strip. *Int. J. Fract.* **167**, 57–70 (2011).
- Corson, F., Adda-Bedia, M., Henry, H. & Katzav, E. Thermal fracture as a framework for quasi-static crack propagation. *Int. J. Fract.* **158**, 1–14 (2009).
- Zheng, Y., Bai, H., Huang, Z., Tian, X., Nie, F., Zhao, Y., Zhai, J. & Jiang, L. Directional water collection on wetted spider silk. *Nature* **463**, 640–643 (2010).

- 19 Bai, H., Tian, X., Zheng, Y., Ju, J., Zhao, Y. & Jiang, L. Direction controlled driving of tiny water drops on bioinspired artificial spider silks. *Adv. Mater.* **22**, 5521–5525 (2010).
- 20 Quéré, D., Di Meglio, J. M. & Brochard-Wyart, F. Spreading of liquids on highly curved surfaces. *Science* **249**, 1256–1260 (1990).
- 21 Callister, W. D. & Rethwisch, D. G. *Fundamentals of Materials Science and Engineering: An Integrated Approach* 312–314 (John Wiley & Sons, United States, 2011).
- 22 Ye, T., Suo, Z. & Evans, A. G. Thin film cracking and the roles of substrate and interface. *Int. J. Solids Struct.* **29**, 2639–2648 (1992).
- 23 Vella, D., Bico, J., Boudaoud, A., Roman, B. & Reisc, P. M. The macroscopic delamination of thin films from elastic substrates. *Proc. Natl Acad. Sci. USA* **106**, 10901–10906 (2009).
- 24 Hibbitt, D., Karlsson, B. & Sorenson, P. *ABAQUS User's Manual, Version 6.5.1* (HKS Inc, Providence, RI, 2006).
- 25 Griffith, A. A. The phenomena of rupture and flow in solids. *Philos. Trans. R. Soc. London Ser. A* **221**, 163–198 (1921).
- 26 He, M. Y. & Hutchinson, J. W. Crack deflection at an interface between dissimilar elastic materials. *Int. J. Solids Struct.* **25**, 1053–1067 (1989).
- 27 Broberg, K. B. *Cracks and Fracture* 45–623 (Academic Press, London, 1999).
- 28 Folias, E. S. A circumferential crack in a pressurized cylindrical shell. *Int. J. Fract.* **3**, 1–11 (1967).
- 29 Sih, G. C. & Chen, E.P. in *Mechanics of Fracture, Plates and Shells with Cracks* Sih, G. C. (ed.) Vol. 3, 231–272 (Noordhoff International Publishing, Leyden, 1977).
- 30 Solanki, P. R., Kaushik, A., Agrawal, V. V. & Malhotra, B. D. Nanostructured metal oxide-based biosensors. *NPG Asia Mater.* **3**, 17–24 (2011).
- 31 Kamiya, T. & Hosono, H. Material characteristics and applications of transparent amorphous oxide semiconductors. *NPG Asia Mater.* **2**, 15–22 (2010).
- 32 Chattopadhyay, S., Chen, L. C. & Chen, K. H. Energy production and conversion applications of one-dimensional semiconductor nanostructures. *NPG Asia Mater.* **3**, 74–81 (2011).



This work is licensed under the Creative Commons Attribution-NonCommercial-No Derivative Works 3.0 Unported License. To view a copy of this license, visit <http://creativecommons.org/licenses/by-nc-nd/3.0/>

Supplementary Information accompanies the paper on the NPG Asia Materials website (<http://www.nature.com/am>)